Supporting Material for:

Imaging of optically active defects with nanometer resolution

Jiandong Feng[1], Hendrik Deschout[1], Sabina Caneva[2], Stephan Hofmann[2], Ivor Lončarić[3], Predrag Lazić[3] and Aleksandra Radenovic[1]

[1]*Laboratory of Nanoscale Biology, Institute of Bioengineering, School of Engineering, EPFL, 1015 Lausanne, Switzerland*
[2]*Department of Engineering, University of Cambridge, JJ Thomson Avenue, CB3 0FA Cambridge, United Kingdom*
[3]*Institut Ruđer Bošković, Bijenička 54, 10000 Zagreb, Croatia*

**Correspondence should be addressed jiandong.feng@epfl.ch and aleksandra.radenovic@epfl.ch*

Supporting Information

Table of contents

1. Sample preparation 2
1.1 CVD growth 2
1.2 Transfer 2
2. Imaging conditions 2
2.1 Microscope setup 2
2.2 Imaging 3
2.3 Localization procedure 3
2.4 Counting 3
3. Supporting information figures 4
4. Defect electronic band diagrams 13
5. References 18

SI Text

1. Sample preparation

1.1 CVD growth

The h-BN samples are grown under same conditions described elsewhere[1]. Briefly, as-received Fe foil (100 μm thick, Alfa Aesar, 99.99% purity) is loaded in a customized CVD reactor (base pressure $1x10^{-6}$ mbar). The foils are exposed to 4 mbar of NH_3 during heating to 900 °C. Subsequently, the NH_3 is removed and borazine $(HBNH)_3$ is introduced into the chamber through a leak valve from a liquid reservoir. After growth (45-90 s borazine exposure at $6x10^{-4}$ mbar and 900 °C) the heater is switched off and the foils are cooled in a vacuum.

1.2 Transfer

The h-BN domains are transferred onto SiN_x membranes using the electrochemical bubbling method[2]. A polymer support layer is deposited onto the h-BN/Fe by spin coating poly(methyl methacrylate) (PMMA) at 5000 rpm for 40 s. The samples are placed in a NaOH bath (1M) and are contacted with a Pt wire that acts as the cathode, while another Pt wire (anode) is immersed in the electrolyte. During electrolysis, H_2 bubbles are generated at the h-BN/Fe interface, lifting the h-BN/PMMA film from the substrate. The film is subsequently rinsed in DI water and scooped with the target substrate, where it is allowed to dry. The PMMA is removed by immersing the sample in acetone overnight, followed by a rinse in IPA. Annealing at 400 ^{0}C under Ar flow is further used to remove remaining surface contamination.

2. Imaging conditions

2.1 Microscope setup

Imaging was carried out on a custom-built microscope that was described previously[3, 4]. Briefly, two laser sources were used for excitation: a 100mW 488 nm laser beam (Sapphire, Coherent) and a 100mW 561 nm laser beam (Excelsior, Spectra Physics). The laser beams were combined using a dichroic mirror (T495lpxr, Chroma) and sent through an acousto-optic tunable filter (AOTFnC-VIS-TN, AA Opto-Electronic). Both laser beams were focused into the back focal plane of an objective (UApo N ×100, Olympus) with a numerical aperture of 1.49 mounted on an inverted optical microscope (IX71, Olympus). Excitation and fluorescence light were separated by a filter cube containing a dichroic mirror (493/574 nm BrightLine, Semrock) and an emission filter (405/488/568 nm StopLine, Semrock). The fluorescence light was detected by an EMCCD camera (iXon DU-897, Andor) with a back-projected pixel size of 105 nm. An optical system (DV2, Photometrics) equipped with a dichroic mirror (T565lpxr, Chroma) was used to split the fluorescence light into a green and red color channel that were each sent to a separate half of the camera chip.

2.2 Imaging

Before imaging, 100 nm gold nanospheres (C-AU-0.100, Corpuscular) were added to the chip for lateral drift monitoring. The addition of fiducial markers was done by incubating the chip at least 15 minutes with a droplet of the gold nanospheres diluted up to 10 times in water. After removing the droplet, the chip was baked at 120 °C for at least 10 minutes and rinsed with water. The chip was placed upside down on a 25 mm diameter round cover slip (#1.5 Micro Coverglass, Electron Microscopy Sciences) that was cleaned with an oxygen plasma for 5 minutes. Imaging was performed in water at room temperature. Excitation in the red channel was done at 561 nm with ~20 to ~30 mW power (as measured in the back focal plane of the objective). Excitation in the green channel was done at 488 nm with ~10 mW power. The gain of the EMCCD camera was set at 100 and the exposure time to 50 ms. For each experiment, at least 20,000 camera frames were recorded. Dual-colour imaging was performed by first acquiring at least 10,000 camera frames in the red channel, and subsequently recording at least 10,000 camera frames in the green channel. Gold nanospheres were imaged to co-register the two color channels a posteriori. Axial drift correction was ensured by a nanometer positioning stage (Nano-Drive, Mad City Labs) driven by an optical feedback system[5]

2.3 Localization procedure

The camera frames were analyzed by a custom written algorithm (Matlab, The Mathworks) that was adapted from an algorithm that was described elsewhere[3, 4]. First, a Gaussian filter and subsequently the Gaussian curvature filter[5] was applied to each frame separately. This yields an image of the uneven background consisting of triangular structures that correspond to fluorescence from the bulk hBN. This background image was subtracted from the original frame (after applying the same Gaussian filter), resulting in an image of the emitters on a uniform background. Only peaks with an intensity of at least 4 times the background were considered to be emitters. These peaks were fitted by maximum likelihood estimation of a 2D Gaussian point spread function (PSF)[6] and the localization precision was obtained from the Cramér-Rao lower bound[7]. Drift was corrected in each frame by subtracting the average position of the gold nanospheres from the emitter positions in that frame. Co-registration of the two color channels was done using a second order polynomial transformation that was derived from the localizations of the gold nanospheres visible in both color channels. The SMLM images were generated as a probability map by plotting a 2D Gaussian PSF centered on each fitted position with a standard deviation equal to the corresponding localization precision. Only positions with a localization precision below 30 nm were plotted.

2.4 Counting

Determining the number of emitters by simply counting the localizations yields an overestimation in case there is "blinking," i.e. the same emitter reappears once or several times. We corrected this possible error by borrowing a method that was developed in the context of counting photo-activatable fluorescent proteins[8]. The idea is that two different localizations are considered to originate from the same blinking event if they are close enough in space and time. Merging these localizations based on a suitable spatial and temporal threshold, therefore, results in a corrected number of localizations. To account for the localization precision, the spatial threshold was calculated from the Hellinger distance, which was taken equal to 0.9[4]. The temporal threshold was varied between multiples of the camera exposure time, i.e. the first five multiples[8], yielding five different corrected localization numbers. A semi-empirical model was fitted to these values as a function of the temporal threshold, resulting in a

final corrected localization number[8]. The model assumes that the emitters go from an off-state to an on-state, and subsequently they either reversibly go to a dark state or irreversibly to a photobleached state.

3. Supporting information figures

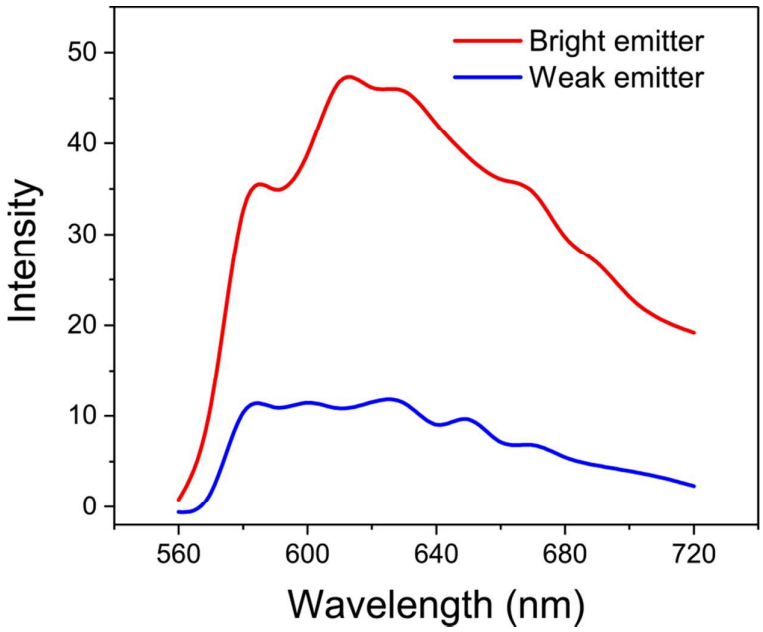

Figure S1. Emission spectra of 2 types of defects taken under 561 nm excitation.

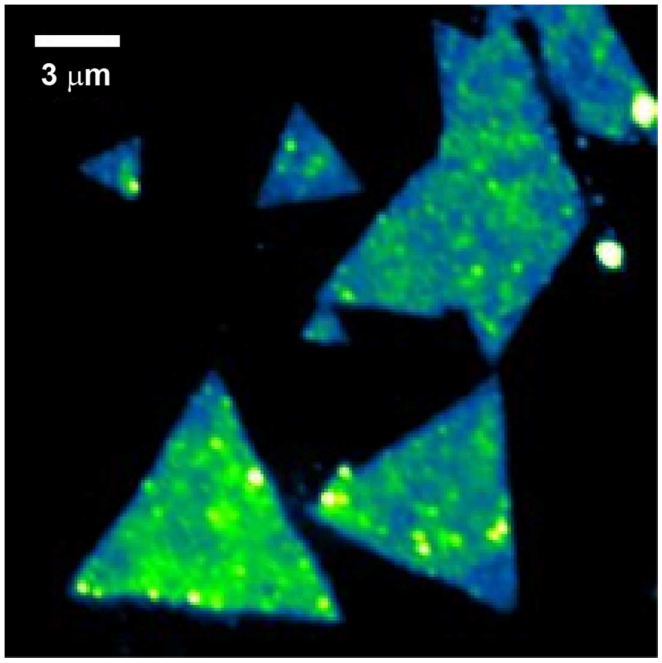

Figure S2. Generated diffraction-limited image by summing all 20,000 frames, corresponding to the SMLM image shown in **Figure 2a**.

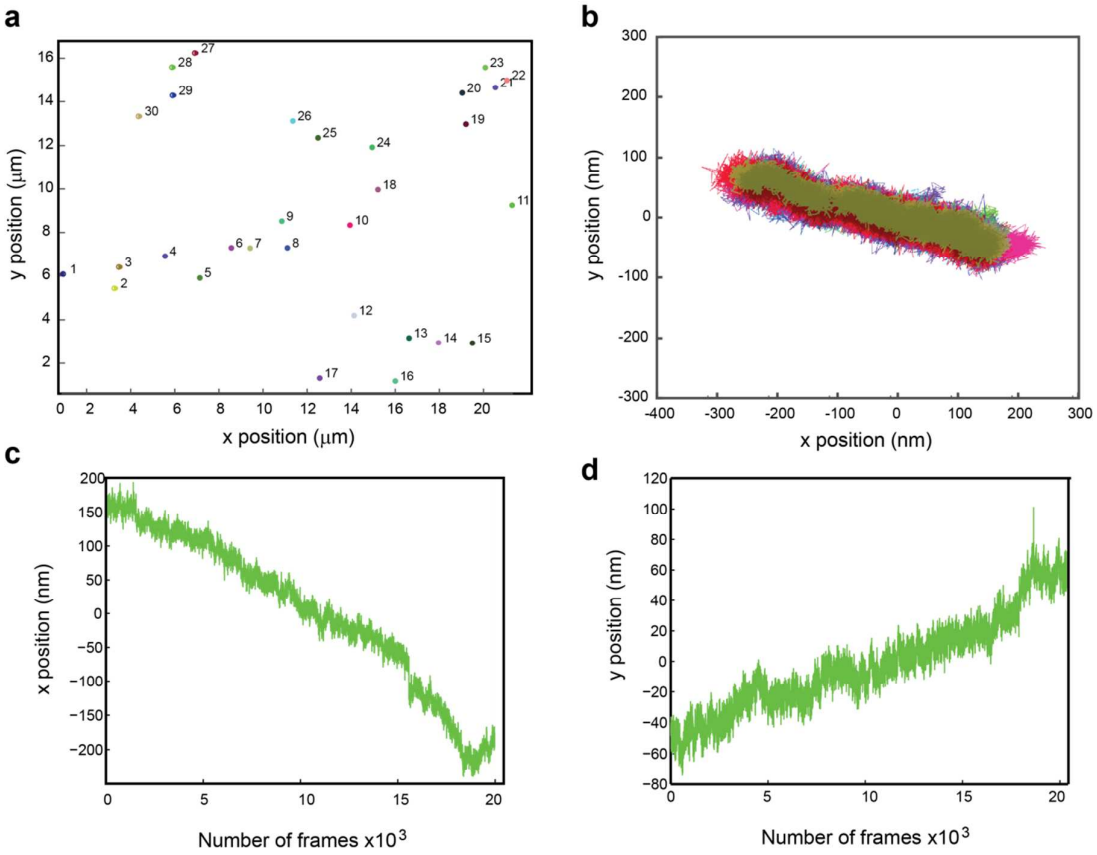

Figure S3. Drift correction using fiducial markers. **(a)** Corrected position of 30 fiducial markers (100 nm gold nanoparticles- from which 27 fiducial markers are used for drift correction). **(b)** Drift trajectories of all 27 fiducial markers over 20,000 frames. **(c)** and **(d)** x,y stage drift as a function of frame numbers.

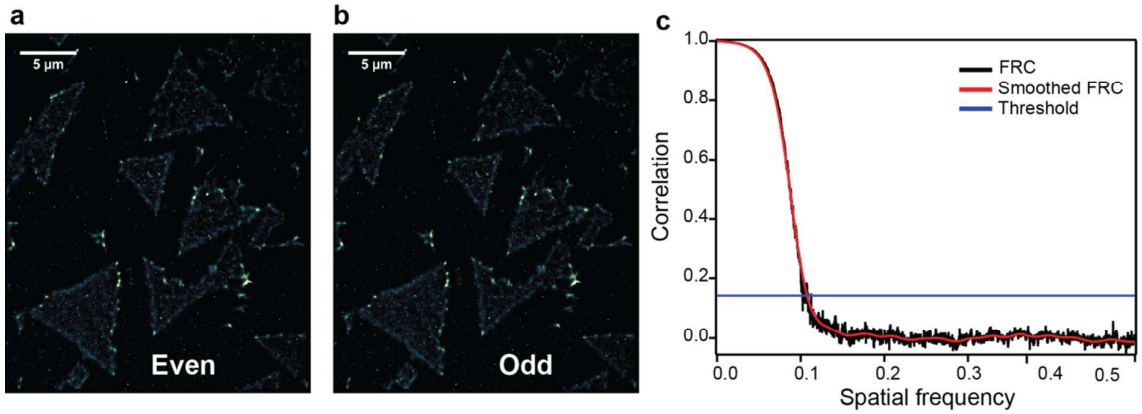

Figure S4. FRC resolution analysis. **(a)** Generated SMLM image using even number frames. **(b)** Generated SMLM image using odd number frames. Total number of frames: 20,000. Image conditions: DI water, 561 nm laser. **(c)** FRC curve indicates the decay of the correlation with spatial frequency. The image resolution (46 nm) is obtained using the inverse of the spatial frequency where FRC curve drops below the threshold 1/7.

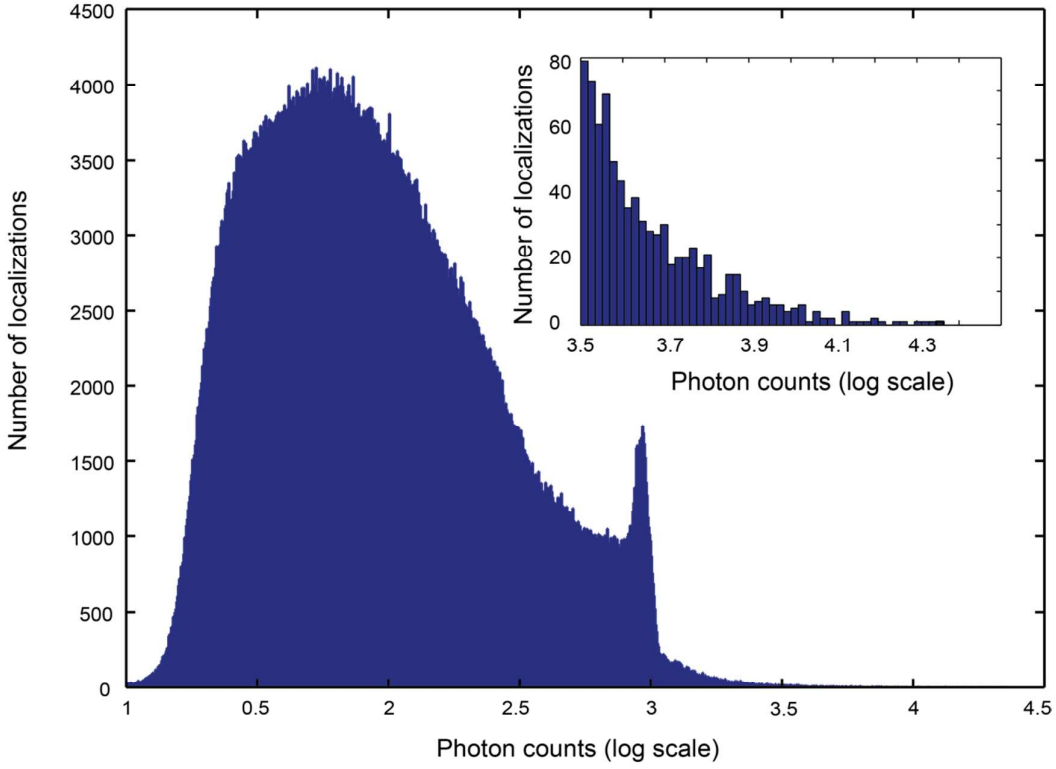

Figure S5. Log-scale histogram of photon counts for the results shown in **Figure 2a**. Insets show zoomed region of high photon counts. Distribution in photon counts indicates the coexistence possibility of multiple types of defects.

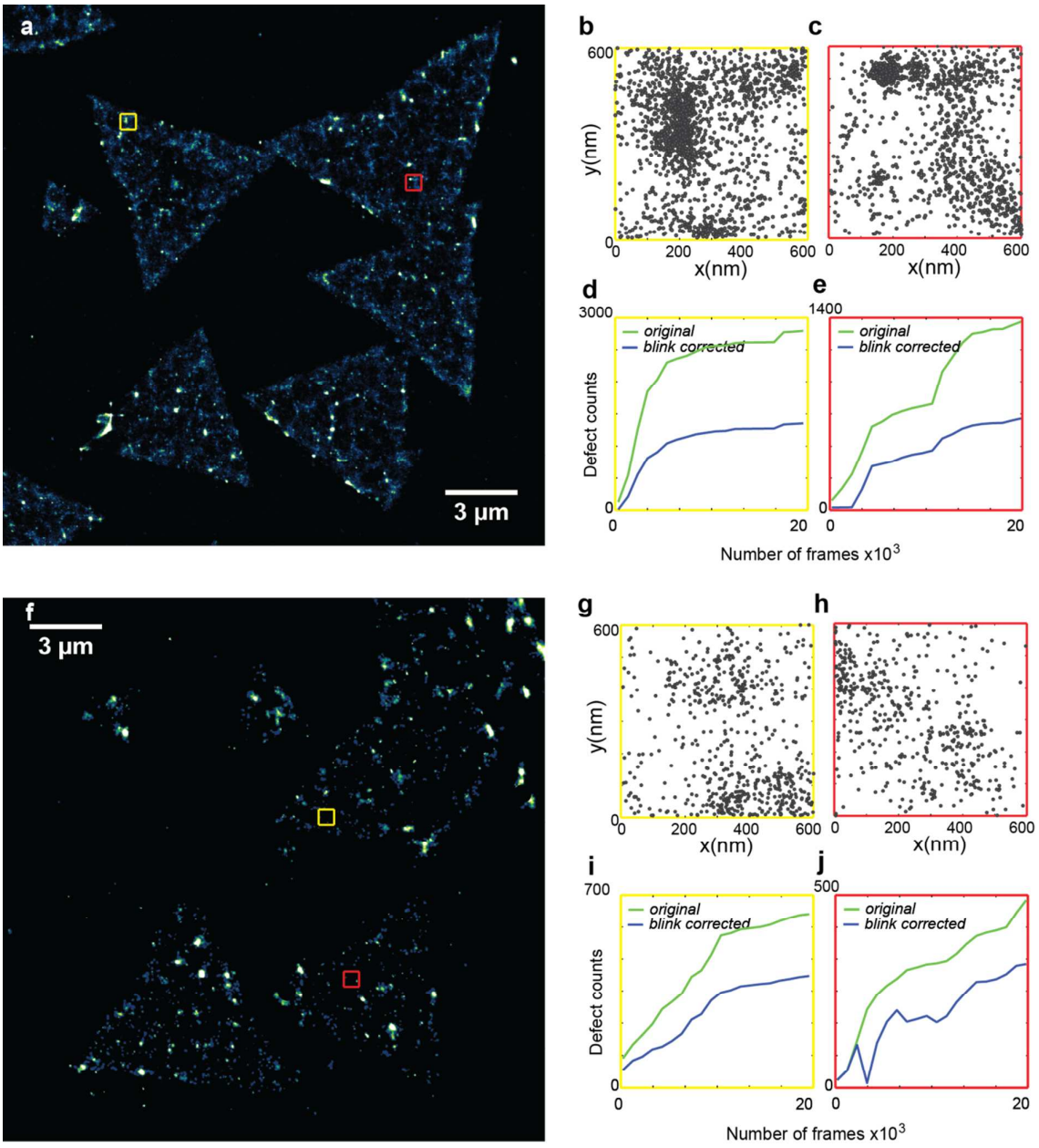

Figure S6. SMLM imaging of defects in h-BN under basic and acidic conditions. **(a)** SMLM image acquired under basic environment (pH 11, water). **(b)** and **(c)** Selected ROI in **a** and corresponding counting results **d** and **e**, respectively. The average defect density is from 1018 μm^{-2} (blink corrected) to 1648 μm^{-2} (total localizations). **(f)** SMLM image acquired under acidic environment (pH 3, water). **(g)** and **(h)** Selected ROI in **f** and corresponding counting results **i** and **j**, respectively. The average defect density is from 198 μm^{-2} (blink corrected) to 307 μm^{-2} (total localizations).

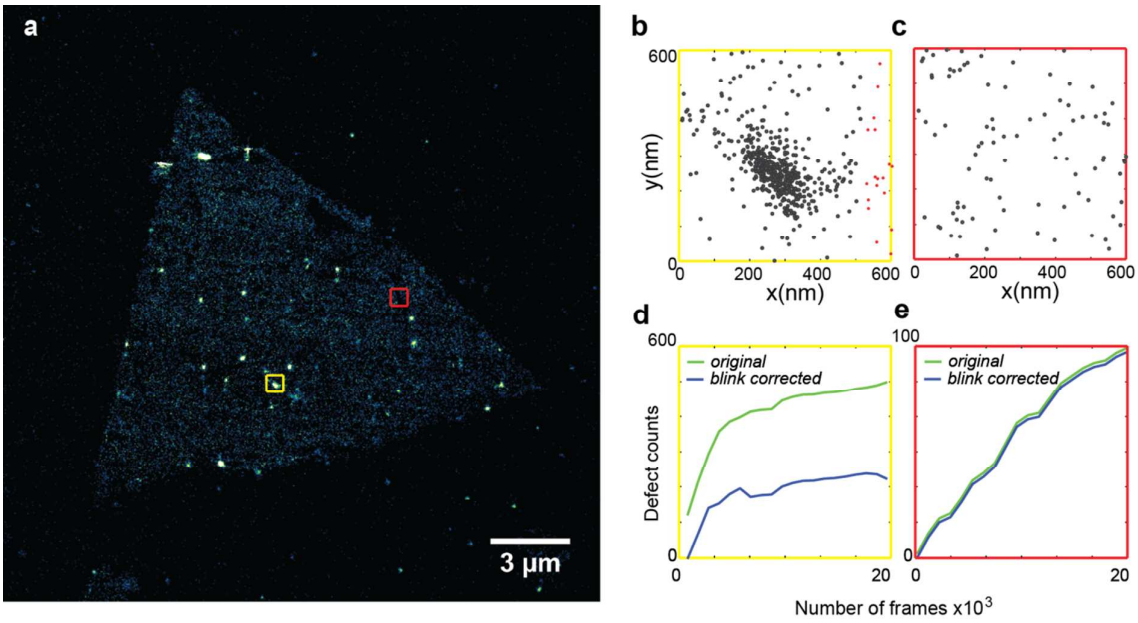

Figure S7. SMLM imaging of defects in h-BN after surface deposition. **(a)** SMLM image of h-BN sample where defects are sealed by depositing 2 nm Al_2O_3 with atomic layer deposition. **(b)** and **(c)** Selected ROI in **a** and corresponding counting results **d** and **e**, respectively. The average defect density is from 201 μm^{-2} (blink corrected) to 253 μm^{-2} (total localizations).

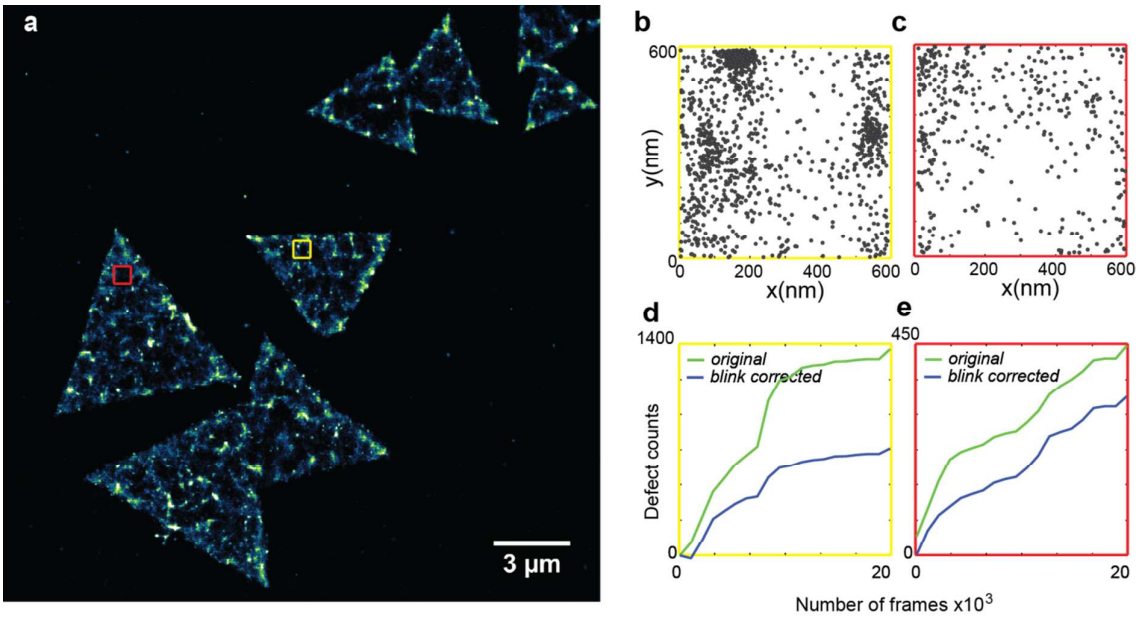

Figure S8.SMLM imaging of defects in h-BN under isotopic solvent conditions. **(a)** SMLM image of defects in h-BN in D_2O solvent. **(b)** and **(c)** Selected ROI in **a** and corresponding counting results **d** and **e**, respectively. The average defect density is from 2186 μm^{-2} (blink corrected) to 4132 μm^{-2} (total localizations).

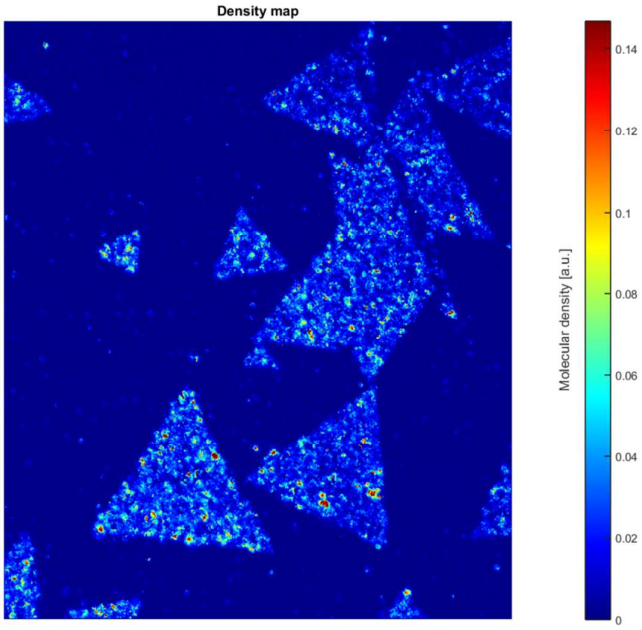

Figure S9. Balanced super-resolution optical fluctuation (bSOFI) images obtained from the same raw image sequences as in **Figure 2a.**

4. Defect electronic band diagrams

Electronic structure of vacancies in monolayer h-BN has previously been studied by Attaccalite et al.[9], Li et al.[10], and Tran et al.[11]. Attaccalite et al. used both simple and rather inaccurate local density approximation (LDA) to density functional theory (DFT) and complex but usually very accurate the so-called GW/BSE theory. Li et al. and Tran et al. used generalized gradient approximation (GGA) to DFT, which in this case gives similar results to LDA. From these studies at LDA or GGA level, it is known that several type of defects have energy levels that can result in optically active transitions with energies of transition of around 2 eV that are observed in our and previous experiments. This is clearly shown in Figure 4 of Ref. 11 for N monovacancy and B vacancy with the N atom shifted over into the empty site (N_BV_N), and also in Figure 6 of Ref. 10 for B monovacancy, N monovacancy, divacancy and N_BV_N. However, it is well known that LDA and GGA have a tendency to underestimate band gaps of insulators, and therefore their predictions of optical properties of insulators are rather inaccurate[12]. Additionally, DFT neglects excitonic effects. Band gap problem of LDA/GGA can be corrected by the so-called GW method, and excitonic effects can be included by solving the Bethe-Salpeter equation (BSE). Attaccalite et al. performed such calculation for B monovacancy, N monovacancy, and divacancy. Not taking into account excitonic effects, the lowest optically relevant transitions in GW for B monovacancy was obtained at 3.5 eV and for N monovacancy at 4 eV. When excitonic effects were included (GW/BSE), Attaccalite et al. predict that the lowest optical peak for B monovacancy should be at around 3.3 eV and for N monovacancy at 2.7 eV. The GW/BSE theory is probably the best method for solid state optical spectroscopy simulations, and therefore it is curious that it seems that this theory does not predict any defect related optical peak that would be in agreement with experiments. One could conclude that either neutral monovacancies are not responsible for peaks around 2 eV, or GW/BSE fails significantly for h-BN defects, or the theoretically studied structure of the system does not represent well the experimental conditions. To enlarge and deepen the search for defects observed in experiments we perform calculations for some of the observed defects in TEM images. Instead of using computationally very demanding GW/BSE, we use hybrid DFT functional that is known to largely correct the band gap problem of LDA/GGA[12].

Our TEM images show the uniform orientation of all defects. The most frequent defect is B monovacancy, but several larger vacancies are also visible. Due to these experimental facts, we have performed DFT calculations of B monovacancy and two larger vacancies with the same orientation, 3B+N and 6B+3N. Structures of these defects are shown in **Figure S10**.

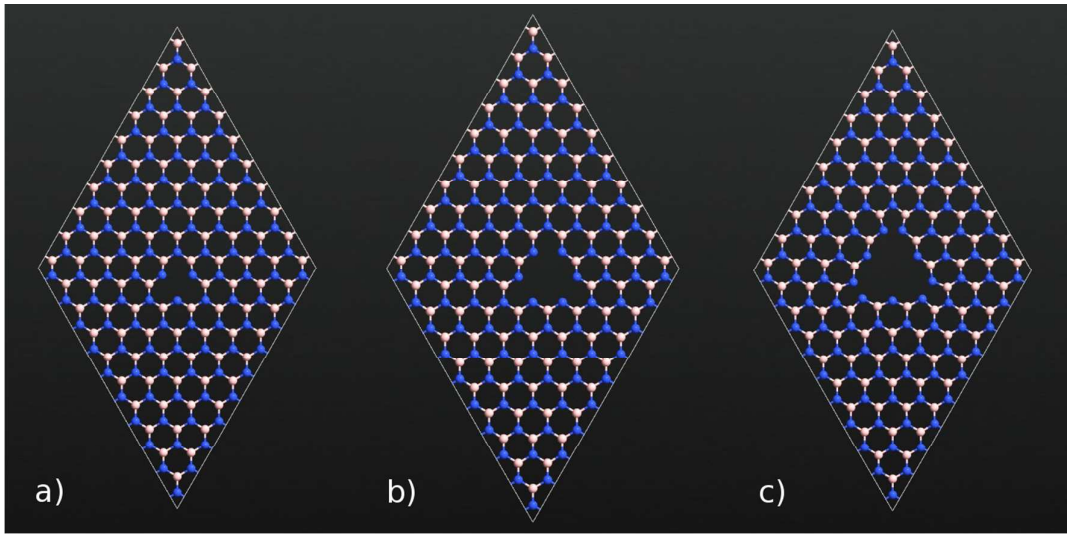

Figure S10. PBE relaxed structure for a) B monovacancy, b) 3B+N vacancy, and c) 6B+3N vacancy.

All our calculations are performed using the plane-wave basis set VASP code[13]. We use 10 × 10 BN unit cell to avoid interaction between defects and Γ point sampling of reciprocal space. For each defect, we first use commonly employed PBE exchange-correlation functional[14] to relax structures and then we perform hybrid DFT calculation using the so-called HSE06 functional[15, 16]. As noted above, it is well-known that ordinary PBE functional usually underestimates band gaps and that it is prone to delocalization errors. As we want to simulate optical properties of defect levels in monolayer BN, both of these errors can severely limit the applicability of PBE to simulate this system. Hybrid functionals that include a portion of exact exchange usually give much more accurate band gaps and delocalization errors are smaller. Our DFT results are shown as band diagrams in **Figure S11** for B monovacancy, **Figure S12** for 3B+N vacancy, and **Figure S13** for 6B+3N vacancy. Additionally, as we connect photo switching of strong emitters, observed in experiments, with charged defects, in **Figure S11** we also show the calculation for charged B monovacancy. Our PBE results are consistent with previous studies[9-11]. We observe large differences between PBE and HSE06 results for all three vacancies. Differences in band gaps are clearly visible both for bulk bands (bulk band gap is around 4.7 eV in PBE calculation and around 6.2 eV in HSE06 calculation) and defect levels. Moreover, there are some vacancy related levels inside the band gap that appear in the HSE06 calculations and not in the PBE calculations and *vice versa*. Due to the reasons stated above, we believe that HSE06 results should be much closer to reality and, therefore, in the following, we base our conclusions on them. To explain the experimental results, we should focus on defect levels that lead to transition energies of around 2 eV. Note that experimentally we measure spectra only in narrow energy range (1.65 eV to 2.75 eV) and, therefore, there might be additional, possibly stronger, optical peaks outside this range that are not seen in experiments.

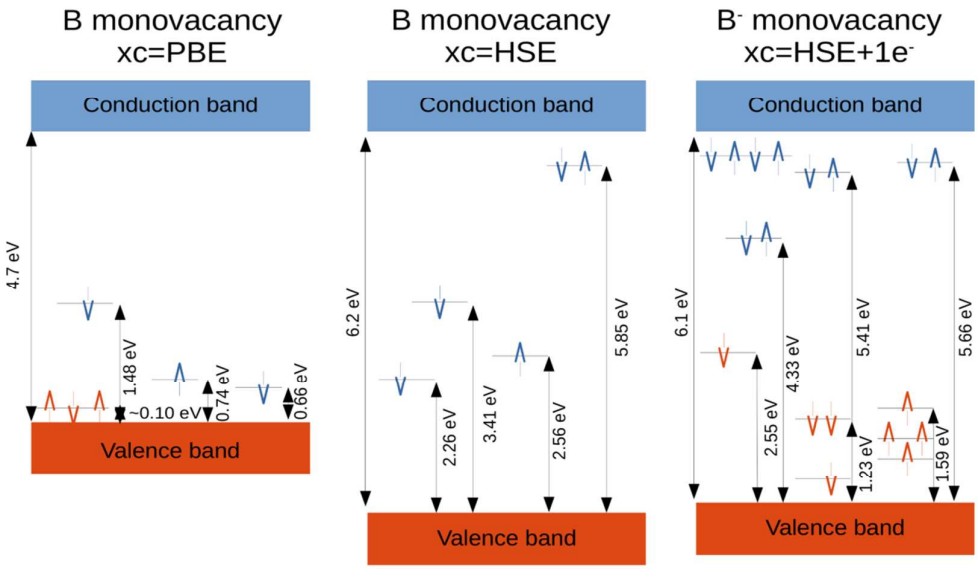

Figure S11. Band diagrams of neutral (PBE and HSE06) and charged (HSE06) B monovacancy. Occupied states are in orange and unoccupied states are in blue.

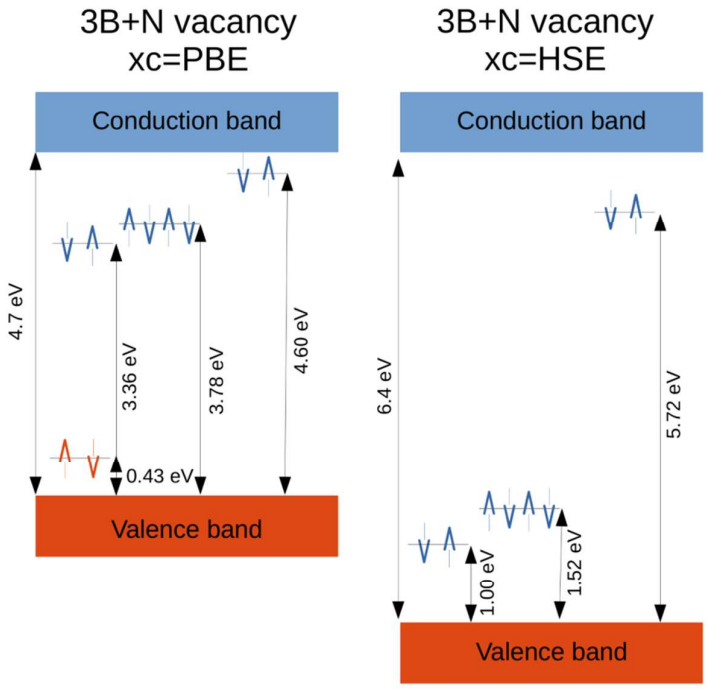

Figure S12. Band diagrams of neutral 3B+N vacancy. Occupied states are in orange and unoccupied states are in blue.

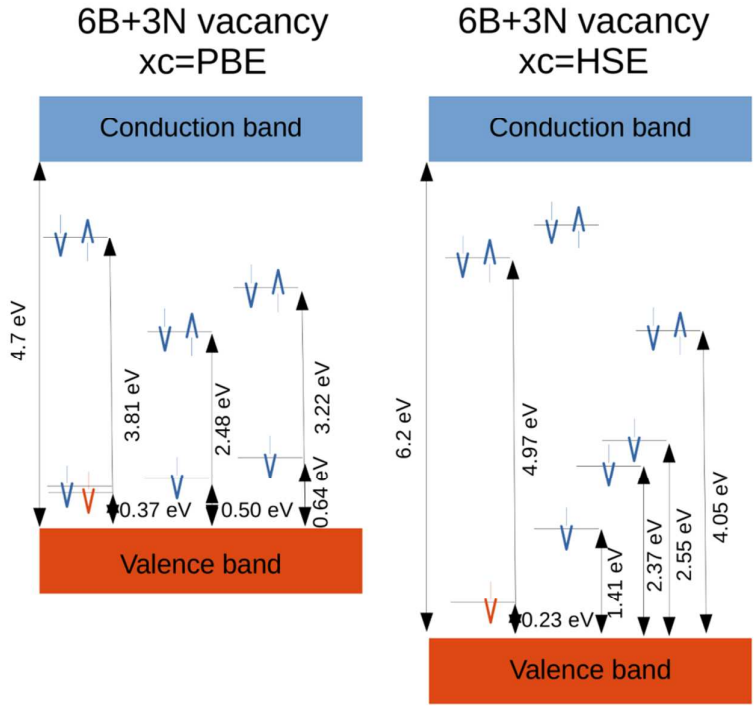

Figure S13. Band diagrams of neutral 6B+3N vacancy. Occupied states are in orange and unoccupied states are in blue.

In addition to available transition energies, photoexcitation and fluorescence spectra also depend on transition strength between two states that is given by dipole transition matrix elements. Therefore, in **Figure S14** we plot spectra that show both transition energies and transition strengths.

Results for each vacancy are listed below:

- **B monovacancy:** B monovacancy is the most common defect in our TEM images and therefore it is the first candidate for the homogeneous fluorescence. In agreement with previous studies, PBE results show three unoccupied defect levels at 0.66-1.48 eV above the valence band (left panel of **Figure S11**). The highest one is responsible for optical transitions to states within valence band with the energy of around 2.3 eV as shown in the left panel of **Figure S14**. Such peak in optical spectra would fit experiments. On the other hand, hybrid functional DFT results (middle panel in **Figure S11**) also show three unoccupied defect levels within bulk band gap but with higher energies of 2.26 eV to 3.41 eV above the valence band. These levels have transition energies toward the top of the valence band that would also be in accordance with the experimental results, especially considering that excitonic effects would lower these transition energies. However, as can be seen in the right panel of **Figure S14**, transition strengths for these transitions are very low and we obtain the same conclusions that were obtained in Ref. [9] with the GW/BSE theory. Namely, there are no significant optical transitions below 3.5 eV, far higher than observed in experiments. These results are puzzling and should be resolved by future measurements and calculations. From the one side, experimentally the most likely candidate for homogenuous emission is supported by PBE calculations that are typically rather inaccurate. From the other side, state of the art theoretical calculations like hybrid functional DFT or GW/BSE do not support it. Before concluding that B monovacancy is not responsible for homogeneous emission, further research is needed keeping in mind that even though GW and HSE are robust methods, it is possible that for some (still unknown) reasons they fail in predicting optical properties of this defect. Additionally, it should be explored whether defect-defect, defect-substrate, and defect-adsorbate interactions that are present in experimental conditions influence the electronic structure of the defect. From an experimental point of view, it would be helpful to have additional measurements in the full range of energies.

- **Charged B monovacancy:** Results for negatively charged B monovacancy (right panel in **Figure S11**) show several additional occupied and unoccupied defect levels within the bulk band gap. The transition from the highest occupied to the lowest unoccupied defect level corresponds to the energy of 1.78 eV. Right panel of **Figure S14** shows a clear peak at this transition energy, which demonstrates substantial transition strength. As this transition is due to the two defect levels within band gap it would be consistent with a single emitter. However, this transition energy is still significantly lower than in experiments, and the difference is larger than typical hybrid functional errors[12]. It should be said that we did not additionally relax the charged defect compared to the neutral defect and therefore the forces on N atoms around the defect are rather large (~1 eV/Å). This could have an impact on the position of the defect levels. As can be seen in **Figure S14**, there is an additional smaller absorption peak at around 2.8 eV that is also due to the transition between two defect levels. Since our results do not include excitonic effects that can easily shift transition energies down for 0.4 eV (see Ref. 9), this peak would be consistent with experiments. All in all, it seems that charged B monovacancy could be responsible for ultra-bright emitters.

- **3B+N vacancy:** HSE band diagram of 3B+N vacancy show unoccupied defect level at 1.0 eV above valence band and double degenerate level at 1.5 eV above valence band. As can be seen in right panel of **Figure S14** transition strengths to the top of the valence band are small and they become large only for transition energies larger than 2.5 eV. Therefore, hybrid functional DFT without considering excitonic effects (that would shift peak to lower energies) predict that 3B+N vacancy have a peak in optical spectra at around 2.8 eV. Due to non-zero dipole transition matrix elements at lower transition energies (toward the top of the valence band), fluorescence is expected to proceed also on lower transition energies. We conclude that 3B+N vacancy would be a good candidate for defect showing homogeneous fluorescence if its density would be high enough.

- **6B+3N vacancy:** For this vacancy, there is a transition with the energy of 1.2 eV which is clearly visible in the right panel of **Figure S11**. In the spectra there is also a peak around 1.5 eV which corresponds to transitions from the defect level at 1.41 eV above valence band to the levels inside the valence band. Some small peaks also exist at transition energies in range 2-2.5 eV that could also be relevant considering the experiments, but the density of this type of vacancy is probably too low.

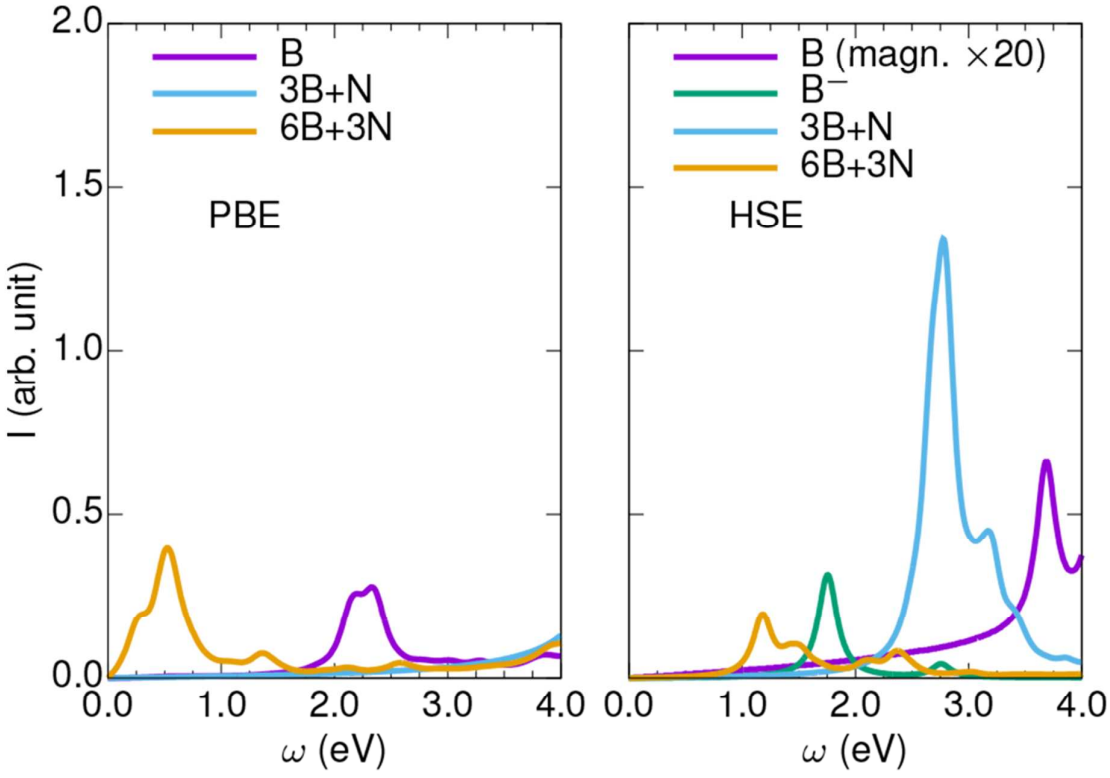

Figure S14. Simulated optical spectra in independent particle approximation calculated with PBE (left panel) and HSE06 (right panel) functional.

5. References

1. Caneva, S.; Weatherup, R. S.; Bayer, B. C.; Blume, R.; Cabrero-Vilatela, A.; Braeuninger-Weirner, P.; Martin, M. B.; Wang, R. Z.; Baehtz, C.; Schloegl, R.; Meyer, J. C.; Hofmann, S. *Nano Lett.* **2016,** 16, (2), 1250-1261.
2. Gao, L. B.; Ren, W. C.; Xu, H. L.; Jin, L.; Wang, Z. X.; Ma, T.; Ma, L. P.; Zhang, Z. Y.; Fu, Q.; Peng, L. M.; Bao, X. H.; Cheng, H. M. *Nat. Commun.* **2012,** 3, 699.
3. Betzig, E.; Patterson, G. H.; Sougrat, R.; Lindwasser, O. W.; Olenych, S.; Bonifacino, J. S.; Davidson, M. W.; Lippincott-Schwartz, J.; Hess, H. F. *Science* **2006,** 313, (5793), 1642-1645.
4. Deschout, H.; Lukes, T.; Sharipov, A.; Szlag, D.; Feletti, L.; Vandenberg, W.; Dedecker, P.; Hofkens, J.; Leutenegger, M.; Lasser, T.; Radenovic, A. *Nat. Commun.* **2016,** 7, 13693.
5. Gong, Y.; Sbalzarini, I. F. In *Local weighted Gaussian curvature for image processing*, Image Processing (ICIP), 2013 20th IEEE International Conference on, 2013; IEEE: 2013; pp 534-538.
6. Mortensen, K. I.; Churchman, L. S.; Spudich, J. A.; Flyvbjerg, H. *Nat. Meth.* **2010,** 7, (5), 377-381.
7. Ober, R. J.; Ram, S.; Ward, E. S. *Biophys. J.* **2004,** 86, (2), 1185-1200.
8. Annibale, P.; Vanni, S.; Scarselli, M.; Rothlisberger, U.; Radenovic, A. *PLoS ONE* **2011,** 6, (7), e22678.
9. Attaccalite, C.; Bockstedte, M.; Marini, A.; Rubio, A.; Wirtz, L. *Phys. Rev. B* **2011,** 83, (14), 144115.
10. Li, X.; Shepard, G. D.; Cupo, A.; Camporeale, N.; Shayan, K.; Luo, Y.; Meunier, V.; Strauf, S. *ACS Nano* **2017,** 11, (7), 6652-6660.
11. Tran, T. T.; Bray, K.; Ford, M. J.; Toth, M.; Aharonovich, I. *Nat. Nanotechnol.* **2016,** 11, (1), 37-41.
12. Crowley, J. M.; Tahir-Kheli, J.; Goddard III, W. A. *J. Phys. Chem. Lett.* **2016,** 7, (7), 1198-1203.
13. Kresse, G.; Furthmüller, J. *Phys. Rev. B* **1996,** 54, (16), 11169.
14. Perdew, J. P.; Burke, K.; Ernzerhof, M. *Phys. Rev. Lett.* **1996,** 77, (18), 3865.
15. Heyd, J.; Scuseria, G. E.; Ernzerhof, M. *J. Chem. Phys.* **2003,** 118, (18), 8207-8215.
16. Paier, J.; Marsman, M.; Hummer, K.; Kresse, G.; Gerber, I. C.; Ángyán, J. G. *J. Chem. Phys.* **2006,** 124, (15), 154709.